

Soft and Integrable Multimodal Artificial Mechanoreceptors Toward Human Sensor of Skin

Seunghwan Seo, Hyun-Min Na, Jin-Yup Kim, Dokyun Kim, Daekyum Kim, Kyoung-Yong Chun,* and Chang-Soo Han*

Herein, the development and characterization of three distinct artificial mechanoreceptor sensors meticulously engineered is reported to emulate human skin. By mimicking the morphology, structure, and response characteristics (including preferential sensitivity, adaptation profile, and frequency response) of biological mechanoreceptors, artificial Meissner, Merkel, and Ruffini sensors capable of detecting pressure, shear, and tensile deformations with high fidelity are successfully fabricated. In situ experiments, designed to mimic physiological conditions, demonstrate that the integrated sensor array, mimicking human fingertips, can accurately discriminate seven Braille characters, five distinct surface textures, a grating with ridges, and four-step delivery stages of an object. Furthermore, a woolen glove incorporating 15 multimodal sensors are developed, which exhibits enhanced classification capabilities for eight objects of varying sizes and surface roughness. Notably, the trimodal sensor integration demonstrates superior recognition speed and precision compared to uni- or bimodal configurations, while also improving tactile identification intuition. This biomimetic mechanoreceptor sensor system demonstrates comprehensive and synergistic recognition of diverse stimuli and objects, potentially overcoming technological limitations in applications requiring human-like tactile perception, such as advanced prosthetics, robotics, and immersive augmented and virtual reality interfaces.

hand work in synchrony to recognize the magnitude and type of different stimuli, enabling complex and precise hand movements. However, despite decades of engineering efforts, artificial tactile systems are still far below the capabilities of biological sensory organs.^[5–14] Human tactile perception, especially the ability to discern and manipulate objects through touch in darkness, relies intricately on a vast array of tactile sensors distributed in our hands. Decades of diverse and exhaustive research have dissected the biological and physiological intricacies governing these sensors. Key components of tactile perception, including Merkel disc (MD), Meissner corpuscle (MC), Ruffini ending (RE), and Pacinian corpuscles (PC), have been extensively studied in biological aspects. These mechanoreceptors play a crucial role in interpreting a wide range of tactile stimuli, from subtle object manipulation to Braille reading.^[15–18] Specifically, MD and RE demonstrate slow adapting (SA), continuously relaying signals in response to prolonged stimuli, while MC and PC, with their rapid adapting (RA) attributes, fire signals in the face of dynamic stimulus shifts.^[16,19–23] The unique

structural modifications of these mechanoreceptors in response to external stimuli activate ion channels coupled to neurons, leading to the generation of ion-mediated signals. Furthermore, the distinct mechanical structure of these receptors determines their preferential responsiveness to different types of mechanical stimulation, providing inspiration for engineering exploration.

Moreover, it is through a harmonious symphony of these mechanoreceptors that the brain deciphers and identifies tactile stimuli, affording us the profound ability to glean insights into the feeling intricacies during tactile interactions with surrounding environment, founded upon the information collected from the signals generated by these receptors. While artificial mechanoreceptors have been recently explored, significant disparities persist between their biological and artificial counterparts. The collaborative working between artificial MD and MC, each possessing a distinct adapting profile and preferential response to the stimulus, is crucial in identifying the touch,^[15,24] but existing research primarily focuses on adapting patterns, emphasizing static and dynamic pressure detection. Recently, it has been developed a comprehensive sensor by partially

1. Introduction

The human sense of touch is renowned for its sophistication and intimacy.^[1–4] Various cutaneous mechanoreceptors in the

S. Seo, H.-M. Na, J.-Y. Kim, D. Kim, D. Kim, C.-S. Han
School of Mechanical Engineering
Korea University
Anam-Dong, Seongbuk-Gu, Seoul 02841, Republic of Korea
E-mail: cshan@korea.ac.kr

S. Seo, H.-M. Na, J.-Y. Kim, D. Kim, K.-Y. Chun, C.-S. Han
Somatosensory Molecular Biomimetics Research Center
Korea University
Anam-Dong, Seongbuk-Gu, Seoul 02841, Republic of Korea
E-mail: kychun@korea.ac.kr

D. Kim
School of Smart Mobility
Korea University
Anam-Dong, Seongbuk-Gu, Seoul 02841, Republic of Korea

 The ORCID identification number(s) for the author(s) of this article can be found under <https://doi.org/10.1002/adfm.202414489>

DOI: 10.1002/adfm.202414489

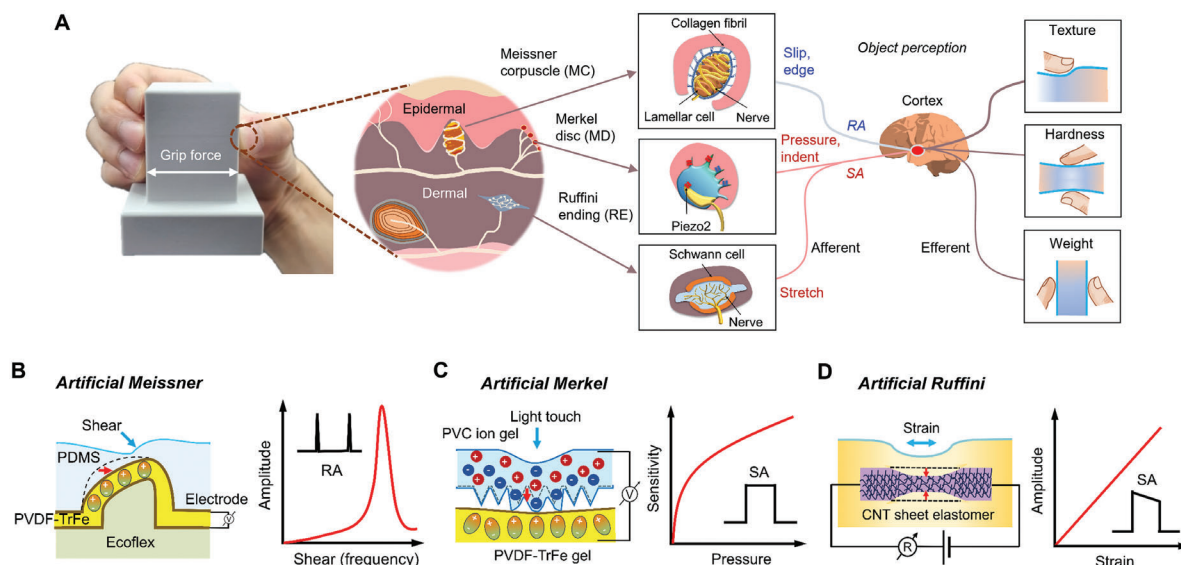


Figure 1. Schematic representation of artificial mechanoreceptors mimicking human skin sensory organs. A) Description of the individual structures, signals, functions, and interconnection mechanisms of mechanoreceptors that operate when gripping an object. It showed representative mechanoreceptors found in the skin simulated in the study, including the Meissner corpuscle (RA signal), Merkel disc (SA signal), and Ruffini ending (SA signal). B) Engineering of MC using piezoelectric mechanism and amplitude curve of MC sensor that appears when a shear force is applied according to the frequency variation. C) MD simulation using ion migration by pressure and piezoelectric charge and nonlinear pressure sensitivity of MD sensor. D) Engineering of RE using piezoresistance of CNT composite sheet and linear output trend of RE sensor according to strain.

implementing the functional characteristics of the typical SA mechanoreceptor, Merkel cell, and the typical RA mechanoreceptor, Meissner corpuscle.^[25] However, there was a limitation that tactile detection was not perfectly implemented based on differentiated data. Also, it was reported about analysis of pressure, shear force, and stretching based on the functional characteristics of Merkel cells and Meissner corpuscles.^[26] Nevertheless, A limitation of this study is that each sensor consists of a simple resistive sensor, which does not capture the detailed features of mechanoreceptor mimicry. Most recently, research has been conducted to artificially replicate the tactile sense based on human touch, but it has been pointed out that there is a mismatch between the function of the developed sensor and the function of the mechanoreceptor.^[27]

This study introduces a novel approach to artificial skin by integrating three distinct sensor modalities that emulate human skin mechanoreceptors. Unlike conventional systems relying solely on single sensor arrays and AI, our multisensory platform enables highly accurate and nuanced object recognition through synergistic interactions between biomimetic mechanoreceptors.

2. Results and Discussion

2.1. Artificial Mechanoreceptors Inspired by Human Skin

The goal of this study is to recognize the characteristics of various objects by mimicking the functions and structures of MD, MC, and RE among the mechanoreceptors in the skin (Figure 1A). For example, when gripping an object, one RA and two SA signals are simultaneously obtained from three mechanoreceptors to recognize object characteristics such as texture, hardness, and weight. To mimic mechanoreceptors effectively, it is crucial to carefully consider the structure of each receptor, analyzing and understanding

the elements that contribute to its operation (Figures 1 and S1, Supporting Information). A brief explanation of the structure and operating mechanism simulated in this study is as follows. First of all, the characteristic structure of the dermal papilla where MC is present, which is known to be sensitive to shear stress, was designed by simplifying it into a dome shape at the interface between the Ecoflex and polydimethylsiloxane (PDMS) of the Meissner sensor (Figure 1A,B). MC responds sensitively to shear forces according to frequency changes, and the signal generated is RA from the. Next, MD, responsive to light pressure, functions as a receptor generating stimulation signals through Piezo2 channels (Figure 1A). It represents a non-linear relationship with respect to normal pressure. Here, poly(vinylidene fluoride-trifluoroethylene) (PVDF-TrFe, PT) gel layer sparks the initial response and conical polyvinylchloride (PVC) ion gel was instrumental in transmitting signals resembling SA signals (Figure 1C). RE features a dendritic nerve structure within collagen, surrounded by a Schwann cell structure (Figure 1A). Multiwalled carbon nanotubes composite sheet was used to simulate nerves operating within collagen, and the role of Schwann cells was replaced with Ecoflex. RE shows linearity over a certain strain range and the signal type is SA (Figure 1D). The manufacturing process of these artificial skin sensors, named Meissner sensor, Merkel sensor, and Ruffini sensor respectively, can be seen in more detail (Figure S2, Supporting Information).

2.2. Characterization of Individual Sensors Inspired by Biological Mechanoreceptors

First, the characteristics of individual sensors are as follows. Merkel sensor is an ingenious reproduction of the highly

sensitive protrusion-like structure housing piezo2 channel, a prominent feature found in MD situated at the interface of the skin's dermis and epidermis.^[15,28–30] This sensor operates through a mechanism that relies on the ion migration (redistribution) of the PVC ion gel, which is influenced by the electric field generated when the PT gel polarizes in response to pressure stimuli (Figures 2A and S3, Supporting Information).^[31,32] It is important to note that the PVC ion gel, in isolation, lacks the inherent capacity to generate electric fields in response to current flow or voltage differentials induced by external pressure. Consequently, the sensor remains unresponsive to stimulus-related signals, as vividly demonstrated (Figure S4, Supporting Information). To optimize the contact area and sensitivity between the PT gel and PVC ion gel, we have effectively employed a modified conical surface structure, building upon prior work.^[33–35] It exhibits the typical SA response of the Merkel sensor when exposed to varying levels of normal pressure (Figure 2B). The sensitivity of a Merkel sensor, described as the relationship between pressure and voltage changes, manifests as distinct patterns in two different ranges: 0.15 mV kPa^{−1} (<15 kPa) and 0.04 mV kPa^{−1} (<66 kPa) (Figure 2C). This sensitivity profile aligns with established ranges observed in conventional polymer and gel-based pressure sensors.^[31,36–38] Notably, the sensor's response value is contingent not only on the magnitude of the applied force but also on the angle of touch (Figure 2D). With increasing the angle of touch, the SA characteristics persist, albeit with a concurrent decrease in response voltage. This phenomenon is attributed to the reduced contact area between the PT gel and PVC ion gel, alongside the dispersion of the pressure magnitude. This unique attribute provides a heightened level of granularity when the sensor makes contact with an object. Also, the Merkel sensor exhibited an initial response time of ≈0.7 s, reaching 80% of its saturation value (Figure 2E). It demonstrated a nearly instantaneous response to input pressure, aligning with the established pattern observed in conventional gel sensors.^[36,38]

MC is a receptor with bell-shaped morphology nestled within the dermal papillae. This architectural intricacy accommodates RA I afferents, strategically ensconced between Schwann cells residing inside the MC. A well-established prehension in the field is that when mechanical stimuli are applied to the skin and transmitted to the MC via the epidermis, the MC undergoes deformation, consequently eliciting neural spikes from the RA I afferents.^[16,24,39] Notably, this process is facilitated by the differential mechanical characteristics of the epidermis and dermis, allowing for the effective transmission of shear stress and shear-direction vibrations from the skin's surface to the MC.^[40,41] In light of these distinctive attributes, we have engineered the Meissner sensor.

Meissner sensor inspired by MC incorporates a material that is responsive to both pressure and shear forces, effectively utilizing the mechanical responsiveness between two materials (PDMS and Ecoflex) with disparate Young's modulus (Figure 2F). The resultant signal modulation in response to normal pressure is a consequence of the development of piezoelectric properties, contingent upon the extent of deformation within the PT gel layer situated between PDMS and Ecoflex. Remarkably, the characteristic peak in response exhibits stable increments corresponding to the speed of applied pressure (2 ≈10 mm^{−1}s), and it adheres to linear characteristics within this spectrum of pressure speeds

(Figure 2G,H). Furthermore, the Meissner sensor, in addition to its acute responsiveness to normal pressure stimuli, manifests unique response characteristics in the domain of shear response (Figure 2I). A linear vibrator, leveraging the Lorentz force mechanism, was employed to impart shear-direction vibration stimuli. Preserving a constant input current of 500 mA, the vibrational frequency spanned from 5 to 100 Hz. The Meissner sensor demonstrated an RA response reminiscent of the characteristic signal observed in piezoelectric elements, with the output signal value exhibiting a change according to the magnitude of vibration. To evaluate the Meissner sensor's response to vibration, we employed the Fast Fourier Transform to compute the amplitude at each frequency, subsequently comparing it to the output corresponding to the vibration stimulus frequency.

The sensor manifested an escalating response to vibration stimulation from 5 to 35 Hz, followed by a gradual amplitude decrease for vibrations surpassing ≈45 Hz. Notably, the Meissner sensor exhibited its maximum peak response between 35 and 40 Hz. In contrast to the Meissner sensor, the MC shows the response characteristics contingent on the threshold for indentation, rendering direct comparative analysis challenging. Nonetheless, we conducted an indirect juxtaposition, analyzing the electrical output characteristics of the Meissner sensor in response to varying vibration frequencies and comparing them to the mechanical output tendencies of MC under the threshold of indentation (Figure 2J). It is well-established that MC exhibits heightened sensitivity within the 30–50 Hz range,^[23,42] a range remarkably congruent with the observed characteristics in the Meissner sensor. These findings underscore that the Meissner sensor, uniquely responsive to shear stress along the horizontal axis while modulating vibration frequency, echoes frequency characteristics akin to those exhibited by MC.

Biomimetic Meissner sensor has similarities in several aspects such as frequency characteristics, morphological shape, soft materials, and working mechanism (Table S1, Supporting Information). These seem to produce similar frequency characteristics having peak response at 35–40 Hz. Moreover, these features can be adjusted by controlling the sensor's performance which could broaden the application of the Meissner sensor.

RC, situated at a deeper dermal layer compared to MD and MC, functions as a mechanoreceptor specialized in perceiving skin tension and deformation, thereby conveying tactile signals to the SA II afferent.^[16] While the precise operational mechanism of RC remains a subject of ongoing exploration, it is well-established that when the skin undergoes stretching, tension is exerted upon RC, prompting the embedded SA II afferent, ensconced within RC's collagen fibers, to generate a responsive signal.^[43,44] Here, in order to mimic the role of nerve fibers in RC, we have harnessed a MWCNTs sheet, characterized by an increase in resistance in response to tensile stimuli. Ecoflex has been seamlessly infiltrated into the MWCNTs sheet, mimicking the role of collagen fibers and nerves within RC (Figure 2K Section 4; Figure S2C, Supporting Information).

The Ruffini sensor has consistently demonstrated a response profile, maintaining the characteristic SA curve throughout a tensile test encompassing ≈40% deformation (Figure 2L). Furthermore, we have observed that Ruffini sensor delivers a linear output value within the range of tensile forces (Figure 2M).

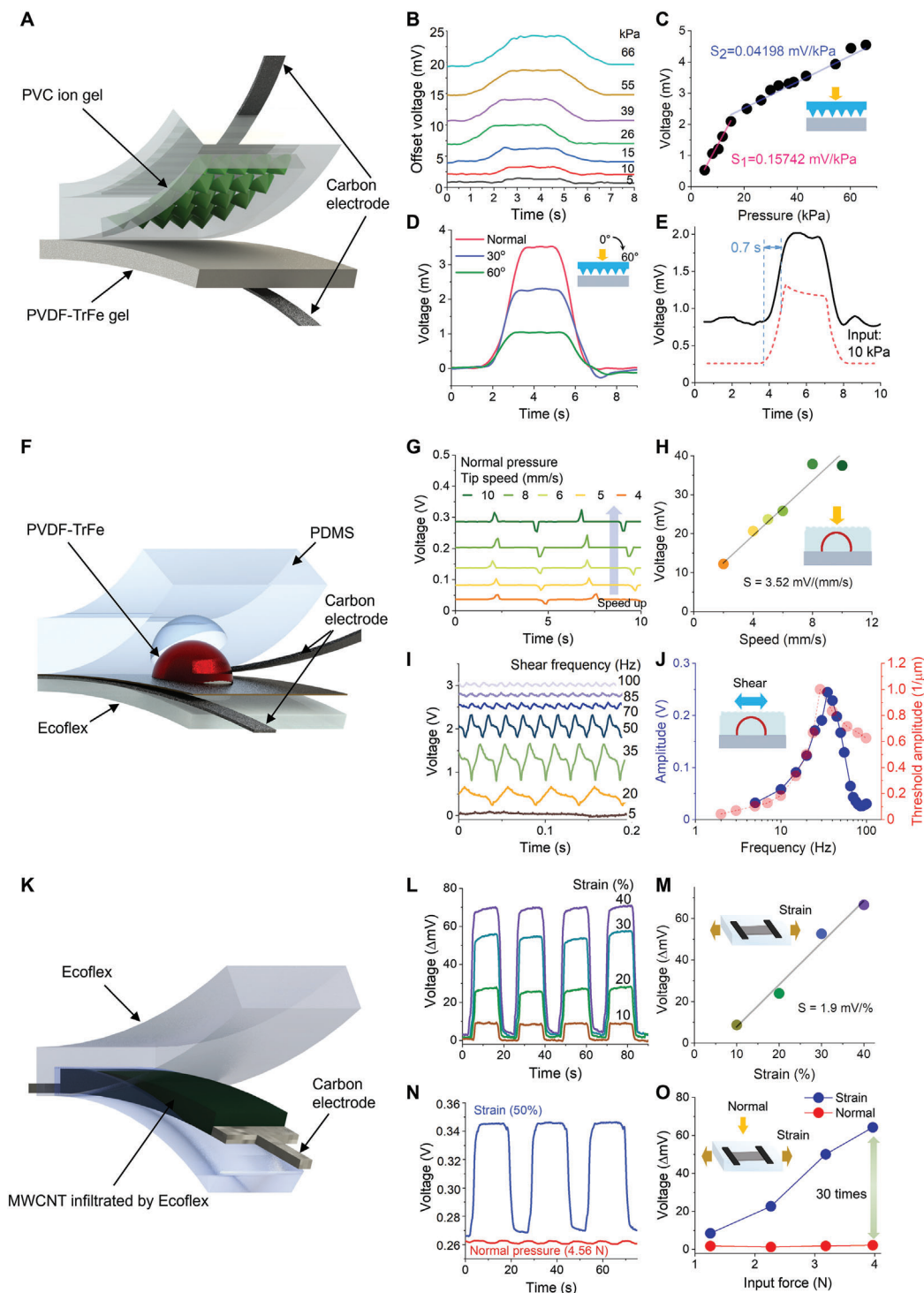


Figure 2. Characteristics of individual artificial skin sensors. A) The signal generation mechanism of the Merkel sensor. External pressure induces polarization in the PVDF-TrFe gel, generating an electric field and facilitating charge transfer in the PVC ion gel. B) Voltage output of the Merkel sensor. C) Sensor sensitivity, categorized into two areas (0.15 mV kPa^{-1} ($<15 \text{ kPa}$) and 0.04 mV kPa^{-1} ($<66 \text{ kPa}$)), indicating the elastic nature of the sensors. D) Change in voltage output concerning the contact angle of the sensor. E) Initial response time of the Merkel sensor. F) Illustration of the operating mechanism of the Meissner sensor in response to external force. G) Response RA signals of the Meissner sensor according to the tip speed at normal pressure. H) Voltage output increases linearly within a certain speed range as pressure speed rises. I) Typical RA peaks of the Meissner sensor according to the shear force. J) The comparison of the Meissner sensor characteristics with the frequency characteristics of biological MC in response to shear force frequency change. K) Illustration of the operating mechanism of the Ruffini sensor in response to strain. L) SA voltage output of the Ruffini sensor according to the strain. M) The correlation of the Ruffini sensor concerning strain change. N) Characteristics of the Ruffini sensor when subjected to vertical pressure and strain. O) Pressure-insensitive Ruffini sensor.

Significantly, Ruffini sensor exhibits marked insensitivity to normal pressure when juxtaposed with its responsiveness to tensile stimuli (Figure 2N). When 50% strain is applied to the Ruffini sensor, the force per tensile area and the force per pressure area are applied equally at 0.126 MPa (Figure S5, Supporting Information). Considering that the overall scale of the Ruffini sensor is $\approx 6 \text{ mm} \times 6 \text{ mm}$, the correspondence force of normal pressure was converted to 4.56 N. The Ruffini sensor demonstrates a significant range of potential difference changes contingent upon the magnitude of the applied tensile force. Conversely, it becomes apparent that the effect of applied normal pressure ($< 4.56 \text{ N}$), is nearly negligible, and there is a notable lack of sensitivity to such pressure. This behavior can be attributed to the mechanics of MWCNTs sheet, serving as the variable resistance component and resisting the normal pressure within the Ruffini sensor, respectively. When subjected to tension, the MWCNTs sheet undergoes substantial mechanical alterations, resulting in conspicuous variations in resistance. Conversely, under normal pressure conditions, the axial strain remains relatively constant, leading to minimal shifts in the resistance of the MWCNTs sheet.^[45] Notably, the output value of the Ruffini sensor in response to tensile forces demonstrates a difference of up to ≈ 30 times when compared to its response to normal pressure at 60% strain (Figure 2O).

While the individual cutaneous sensors developed in the aforementioned sections display distinct signal characteristics, defined by either RA or SA responses originating from diverse mechanical stimuli, it is vital to recognize that achieving tactile perception mirroring human skin through a solitary sensor is intrinsically limited in information capacity and recognition precision. Notwithstanding the diversity of stimuli to which each mechanoreceptor is intrinsically attuned, the human sense of touch is a composite of nerve signals detected by an ensemble of mechanoreceptors, each contributing a unique facet to the tactile experience.^[11,12,23] In light of this perspective, to emulate the human sense of touch, a multimodal integration of sensors with selective and functional disparities, encompassing factors like adapting profiles and tactile responsiveness, becomes indispensable. In our investigation, we have seamlessly integrated the Merkel sensor, the Meissner sensor, and the Ruffini sensor within an Ecoflex and PDMS framework, which have similar stiffness to the dermis and epidermis of the skin, carefully mirroring the anatomical arrangement of these mechanoreceptors within the dermal and epidermal of the skin. The detail of the fabrication is illustrated (Section 4; Figure S6, Supporting Information).

Before performing various surface measurement tests of the integrated sensor, it was confirmed that simultaneously distinct signals can be obtained from the integrated sensor essentially for normal pressure ($\approx 3.5 \text{ N}$). The pressure-sensitive Merkel sensor and Meissner sensor showed typical signals with SA and RA characteristics, respectively, while the pressure-insensitive Ruffini sensor showed weak SA signal characteristics (Figure S7 and Video S1, Supporting Information). A series of comprehensive tactile experiments were conducted, harnessing the collaborative potential of the three advanced sensors. Notably, MD and MC assume central roles in discerning the textural qualities of objects adorned with prominent surface ridges. Integrated sensors are very useful in detecting not only surface texture but also physical properties related to the elasticity of objects. First, an

extra experiment focusing on surface texture analysis was introduced. We investigated the responses of the Merkel and Meissner sensors to a grating with triangular ridges when systematically traversing a surface, oriented either parallel or perpendicular to it (Figure S8, Supporting Information). Evidently, the Merkel sensor exhibited output potential differences characterized by SA properties, triggered by its interaction with surface ridges. Conversely, the Meissner sensor displayed responses that conformed to RA characteristics, underpinned by its piezoelectric properties, which were activated exclusively during momentary height fluctuations induced by the surface's raised features.

In addition, the stability characteristics of the artificial mechanoreceptors demonstrated robust and reliable performance. For the Merkel sensor, stability data are documented in our previous work.^[33] The gel sensor maintained stable operation at 50 Pa and 0.6 Hz under self-powered conditions. Dynamic mechanical analysis (DMA) of the Meissner sensor reveals consistent storage and loss moduli across the testing range, confirming the minimal impact of viscoelastic properties on sensor performance (Figure S9A, Supporting Information). Given that biological Meissner corpuscles typically respond below 50 Hz, stability tests conducted at 50 Hz for 10000 cycles demonstrated consistent amplitude response of the artificial Meissner sensor (Figure S9B, Supporting Information). The Ruffini sensor exhibits stable resistance variations over 12 000 cycles (Figure S9C, Supporting Information), validating the durability of the system. These comprehensive analyses confirm the exceptional stability of all mechanoreceptor components.

2.3. Integrated Sensor Performances for Various Perception Behaviors

In terms of expanding the scope of experimentation, diverse tactile assessments were conducted by layering three sensors in a configuration resembling biological skin. After affixing the integrated sensor attached to the inner surface of the index finger (Figure 3A), various fundamental materials were initially selected to explore whether surface texture could be more accurately identified through signal collection and analysis using the integrated sensor. A photo of the actual manufactured integrated sensor can be seen in the Figure 3B. Signals from three sensors are obtained simultaneously by pressing and rubbing different surfaces (Video S2, Supporting Information), such as glass plate, paper, mesh patterned paper, wool, and sandpaper, three times horizontally ($\approx 2 \text{ kPa}$) at approximately the same speed and interval, and optical images of each surface are presented (Figure S10, Supporting Information). In the exploration of tactile sensing mechanisms, the Merkel and Meissner sensors exhibited distinct signals contingent upon the nature of the surface they encountered.

In addition to textural analysis, the remarkable tactile discernment of the human skin extends to the evaluation of an object's elasticity. When detecting materials with different Young's modulus within elastic substances, such as the skin, the Merkel sensor can provide crucial information compared to the Meissner and the Ruffini sensor (Figure S11A, Supporting Information). These characteristics can be highly suitable for applications like palpation. The sensor's response characteristics were further explored as different-shaped tips contacted the integrated sensor.

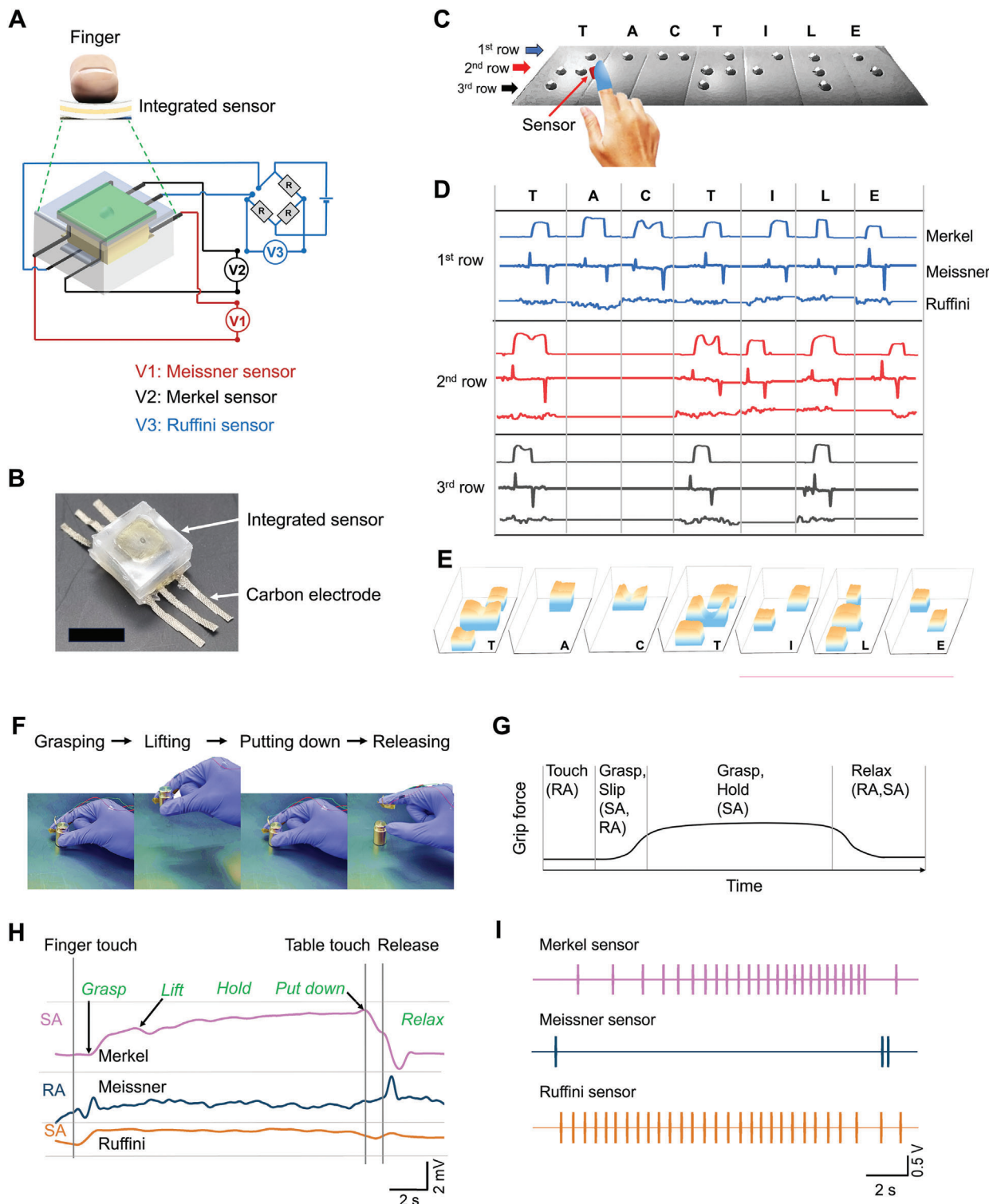


Figure 3. Schematics of the integrated sensor and various behavior characteristics in object recognition. A) Schematics of the structural configuration of an individual integrated sensor. B) The photograph of a manufactured integrated sensor (scale: 1 cm). C) Configuration diagram for the Braille reading experiment using an integrated sensor. The sensor, attached to the finger, systematically scans the letters T, A, C, T, I, L, and E. D) Signals obtained from each individual sensor during Braille reading, color-coded for columns 1 (blue), 2 (red), and 3 (black). E) Transformation of each signal, enabling imaging that closely resembles the actual shape of Braille characters. F) Illustrating the process of grasping and releasing a weight using an integrated sensor attached to a finger. G) Grip force changes over time in grip manipulation of the hand and each representative stimulus force and adaptation type (SA and RA). H) Graphical representation of simultaneous signal changes from individual sensors corresponding to grasping behavior exhibited by the integrated sensor. I) Conversion of the signal changes from the integrated sensor into a spike resembling action potentials, achieved through Matlab.

This was achieved by employing three distinct tip shapes on the pressure-application device: hexahedron, hemisphere, and cone tips (Figure S11B, Supporting Information). The variations in contact area during the application of pressure yielded diverse patterns. The Merkel and the Meissner sensors exhibited SA and RA characteristics, respectively, while the Ruffini sensor displayed minimal signal fluctuations. The distinctive signal alterations observed at the precise moment when the tip disengages from the sensor surface offer a compelling avenue for future investigation. Basically, mechanoreceptors are influenced not only by direct contact with objects but also by deformations occurring on the skin due to body movements. Through simple bending experiments of the integrated sensor, we confirmed that the Ruffini sensor demonstrates the most sensitivity to bending among the integrated sensors, generating significant signal fluctuations within the SA characteristics (Figure S11C, Supporting Information). In the natural domain of mechanoreceptors, RC is not confined to the skin but is also found in the muscle tissue surrounding joints, playing a fundamental role in shaping proprioceptive perception.^[46,47]

The human sense of touch could identify both the texture and precise location of an object simultaneously. To demonstrate these critical features in an artificial tactile system, we performed Braille recognition experiments to read symbolic representations, with Braille characters T, A, C, T, I, L, and E produced in compliance (Figure 3C). The integrated sensor was securely affixed to the tip of the index finger, and systematic scanning of the Braille text was performed in horizontal lines, commencing from the top and progressing in parallel. We precisely measured signal responses to pressure and vibration through tactile interaction with Braille text and compared the signals for three types of sensors. In the case of the Merkel sensor, distinct SA peaks were evident in all instances where Braille characters featured ridges (Figure 3D). Notably, in cases like the second line of T and the first line of C, where the braille ridges are consecutive, the SA peaks tended to continue successively. The Merkel sensor demonstrated a remarkable capability to make clear decisions during Braille recognition, aligning closely with results from existing biological experiments.^[48] The Meissner sensor exhibited typical RA peaks, which varied based on the presence or absence of ridges for each Braille character.

Notably, it generated peaks solely during events of activation and deactivation, resulting in a lower information transmission compared to the Merkel sensor. This exhibits a similar trend to the results observed in biological experiments regarding Braille recognition.^[49] In stark contrast to the signal results obtained from both the Merkel and Meissner sensors, the Ruffini sensor exhibited the most ambiguous response signal during Braille recognition. This observation aligns with the biological findings related to RE, making it challenging to discern Braille letters. Consequently, the study confirmed the specific recognition and differentiation of Braille using three integrated sensors. The systematic horizontal scanning approach employed in our Braille recognition study, utilizing a matrix-based methodology, demonstrates capabilities for comprehensive measurement of diverse Braille configurations beyond the "TACTILE." This approach not only shows the versatility of our sensor system but also provides an intuitive understanding of its tactile-centric characteristics. In Figure 3E, the clearest Braille recognition signal obtained from

the Merkel sensor is presented in a format similar to the signals acquired from biological experiments.^[49] This allows for a direct comparison with actual Braille characters. This figure indicates that the integrated sensor enables precise visual production of the tactile signals obtained, depending on the Braille type.

To figure out the role of mechanoreceptors during the manipulation of the object, biological experiments were performed and they revealed several characteristics of four mechanoreceptors.^[21,39] Likewise, we designed a similar experiment of manipulating the object with a hand. The role of mechanoreceptors in object interaction was explored by attaching the integrated sensor to the index finger and measuring its response during various movements, including grasping, lifting, putting down, and releasing a 100 g weight (Figure 3F). To accurately discern the force applied at the moment of initial contact with an object, during the application of force to grasp the object, at the moment of releasing the object, and when the object is fully released, a combination of interactive signals from both SA and RA receptors is required at each stage (Figure 3G). The Meissner sensor exhibited a maximum RA response upon contact, the Merkel sensor displayed a SA signal during weightlifting, and the Ruffini sensor showed SA responses during finger movement and bending, particularly during weightlifting and pressure application before lifting (Figure 3H). Throughout the contact-maintained lifting process, the Merkel sensor's SA response remained consistent, while the Meissner sensor's RA response was absent. As the weight was raised, the Ruffini sensor showed a SA response due to shear deformation caused by gravity. The gradual increase in the Merkel sensor's static SA response indicated continuous force application to maintain the lifted weight.

Upon placing the weight back down, the Ruffini sensor's response decreased, reflecting the dissipation of shear strain caused by the weight's gravity. Removing the finger holding the weight resulted in an instantaneous RA response in the Meissner sensor, and the responses of the Merkel and the Ruffini sensors, responsible for SA responses, rapidly returned to the initial state. Data from the gripping experiment was modulated into spike signals, which resemble actual afferent responses of human hand grasping,^[50] via Matlab calculation (Figure 3I). Spike modulation code was basically based on the Leaky Integrate and Fire model.^[8] Spike number and density varied with stimulus intensity: the Ruffini and the Merkel sensors with SA properties emitted continuous spikes, while the Meissner sensor with RA properties produced spikes only when lifting and releasing the weight. This versatile multi-mode integrated sensor system played a critical role in recognizing object movement and behavior by providing comprehensive and synergetic information.

2.4. Object Perception by Tactile Glove Sensor System Cooperated with Artificial Intelligent

After verifying the capability of a single integrated sensor to detect various objects, we aimed to present a system that efficiently detects real-life objects and recognizes them through deep learning. Strategically, distributing integrated sensors in a glove was achieved by mimicking the configuration of a human hand. This experiment highlighted the advantages of utilizing diverse tactile information, such as pressure, vibration, and tension, similar to

human skin, over-relying on a single sensor system. Fifteen integrated sensors were strategically placed on the glove, with one at the thumb's tip, two on each finger, and six on the thumb (Figure 4A, Section 4; Video S3, Supporting Information).

The sensor system collected data using a MUX device, and object recognition experiments were conducted with eight categories of objects which were classified according to whether the surface is smooth or rough. Objects were a cushion, a tennis ball, a soccer ball, a handball, and a rugby ball. The experimental protocol involved the following actions. Within the 2–4 s interval, participants gripped and held the object, allowing the sensor to collect data on pressure distribution and information based on the object's shape. Subsequently, within the 4–8 s interval, participants repetitively stroked the object for a predefined duration to gather data related to rubbing and information measured by the sensor, focusing on the surface characteristics of the object. In each trial, the sequence was repeated 50 times for each object category, with data collected at a frequency of 100 Hz. The input data for each trial had a sequence time window of 10 s, resulting in 1000 samples. For each sample at time $t = 1, \dots, 1000$, we defined $x_{\text{Merkel}} = \{x_t^{M1}, x_t^{M2}, \dots, x_t^{M15}\}$, $x_{\text{Meissner}} = \{x_t^{E1}, x_t^{E2}, \dots, x_t^{E15}\}$, and $x_{\text{Ruffini}} = \{x_t^{R1}, x_t^{R2}, \dots, x_t^{R15}\}$ to collect data from the 15 sensors on the glove at every time t .

In this experiment, we employed Long Short-Term Memory (LSTM), a deep learning algorithm well-suited for handling temporal data, for object classification. The deep learning architecture consisted of a 2-layer LSTM, each comprising 128 hidden units. Following the LSTM layers, a fully connected layer with 512 hidden units and Rectified Linear Unit were employed. Another fully connected layer reduced the dimensionality to 8 to classify the categorized objects. We utilized Categorical Cross-entropy loss to minimize the error between the ground truth and predicted object classes. For training and validation, we utilized 40 trials for each object category, reserving 10 trials for testing the model. The training epoch was set to 500, with a batch size of 32. The Adam optimizer was employed, and the learning rate was determined through a grid search starting from 0.0001 with an increment of 0.0001. The model was trained using all combinations of the data from $\{x_{\text{Merkel}}, x_{\text{Meissner}}, x_{\text{Ruffini}}\}$.

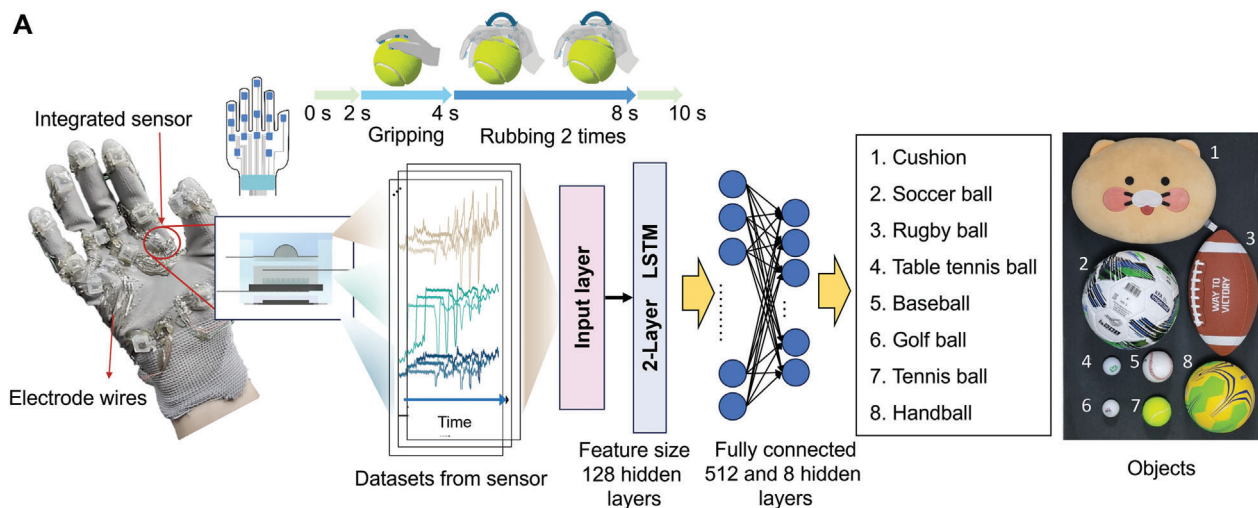
To observe changes in softmax probabilities during the gripping and rubbing stages, we made the following modifications to the deep learning architecture: We removed the final two fully connected layers and fixed the LSTM weights. Following the LSTM layers, we added two fully connected layers, at every time t , with 512 and 8 hidden units, respectively. We trained the architecture with the same training strategy as before. Figure 4B describes the trends observed for each categorized object based on size and surface texture along with softmax probabilities. When considering objects of different sizes, the response of integrated sensors varied depending on the area of sensors that responded. For smaller objects, such as a table tennis ball and a golf ball, the response was primarily limited to the index finger, middle finger, and thumb. Conversely, larger objects engaged a larger area of the sensor system, resulting in a broader response. This variation is depicted using a simple diagram with gradient colors. As outlined in Figure 4A, the protocol for object recognition comprises two main components: 1) gripping and 2) rubbing. The contribution of each component varies depending on whether objects are distinguished by size or texture, which can be discerned through

a comparison of softmax probabilities. As depicted in Figure 4B, when differentiating between objects with a significant disparity in size, such as a rugby ball and a golf ball, the variation in softmax probabilities initiates from the gripping stage. This disparity arises due to differences in the contact area between the object and the glove sensor. Conversely, when distinguishing between objects of similar sizes but different textures, an enhancement in softmax probability is observed not only during the gripping stage but also throughout the rubbing stage. For example, when discerning between a table tennis ball and a golf ball, there is a notable increase in the softmax probability for the golf ball during the gripping stage. While there is a slight uptick in the softmax probability for the table tennis ball, as the experiment progresses to the rubbing stage, minimal change in the softmax probability for the table tennis ball is noted. In contrast, there's significant fluctuation followed by an increase in the softmax probability for the golf ball. This pattern is further accentuated when distinguishing between a baseball and a tennis ball. Due to the distinct characteristics of the leather material of the baseball and the fiber material of the tennis ball, there is a substantial surge in the softmax probability for the tennis ball during the gripping stage. Subsequently, during the rubbing stage, there's notable fluctuation and an increase in the softmax probability for the tennis ball, while there is a tendency for the softmax probability for the baseball to fluctuate and decrease.

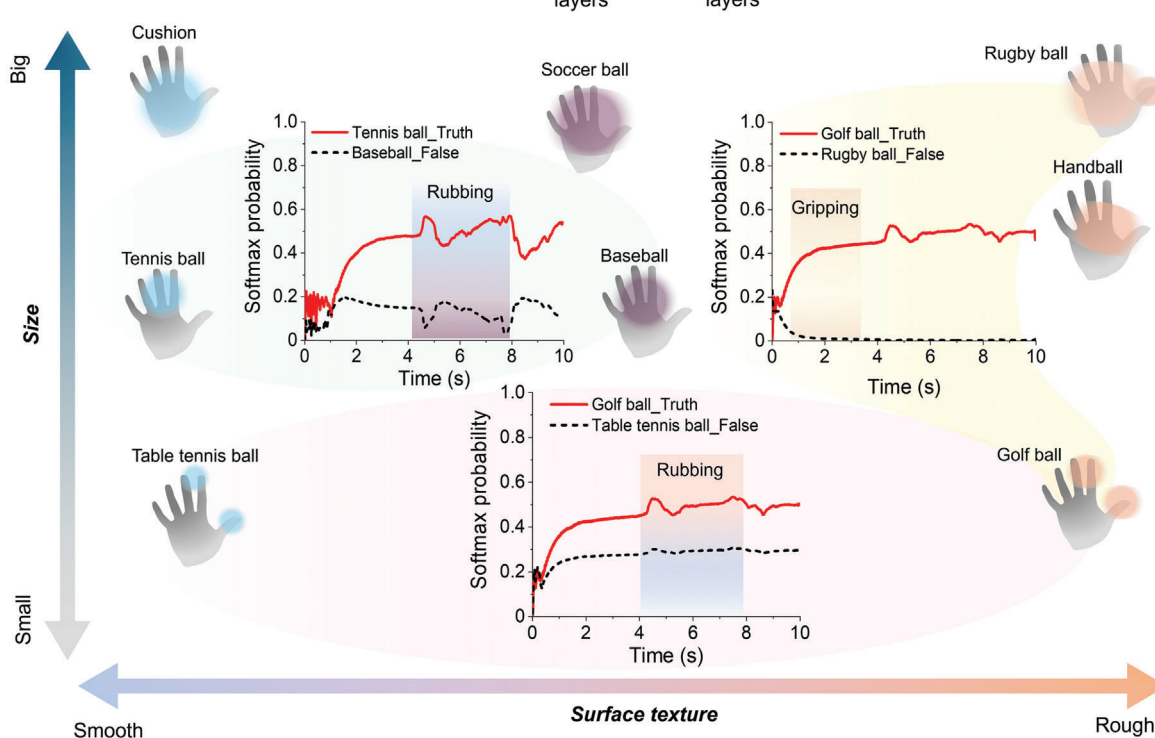
The implemented protocol incorporates complex, sequential grasping-rubbing movements without visual feedback, advancing to replicate human object identification behaviors beyond conventional methodologies.^[27,51–53] While this approach enables discrimination between size-matched objects with varying surface textures, the increased protocol complexity introduces additional signal variability. Enhanced classification accuracy can be achievable through advanced signal processing techniques, including filtering and de-drifting compensation. Furthermore, appropriate scaling of the frequency-specific sensor responses presents an additional optimization pathway for improved classification performance.

Figure 4C presents the comparison of LSTM classification training accuracy for each case. Remarkably, the integrated sensor configuration, incorporating Merkel, Meissner, and Ruffini sensors, achieved the highest accuracy at 90.7%. Additionally, the Merkel sensor alone demonstrated the highest accuracy (79.6%) among cases utilizing a single tactile sensor. However, combining the Merkel sensor with either the Meissner or Ruffini sensor did not result in accuracy improvement. Moving on, Figure 4D displays the confusion chart depicting the outcomes of the object recognition experiment utilizing the integrated sensor. In addition, individual confusion charts for each combination used in the experiment were displayed (Figure S12, Supporting Information). Based on these findings, the study draws the following interpretations: Utilizing single tactile information reveals that the Meissner sensor excels in detecting dynamic stimuli through vibration, the Ruffini sensor excels in detecting stimuli through tension, and the Merkel sensor excels in detecting tactile stimuli through pressure. This leads to higher accuracy in perceiving the mechanical characteristics and shapes of touched objects. However, when dealing with objects of similar sizes but different surface textures, such as a table tennis ball and a golf ball, relatively lower accuracy was observed. Sundaram et al.

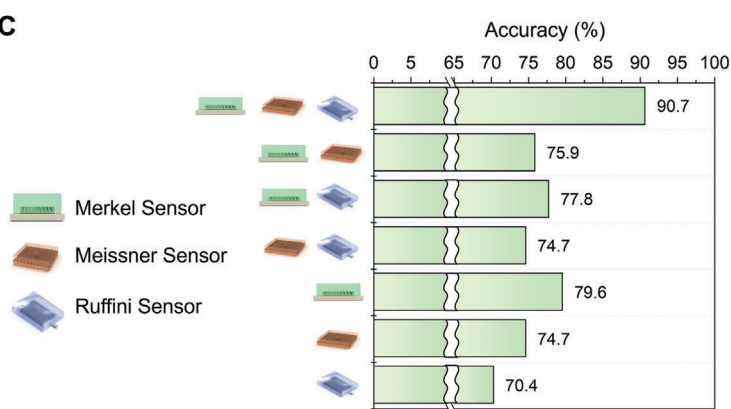
A



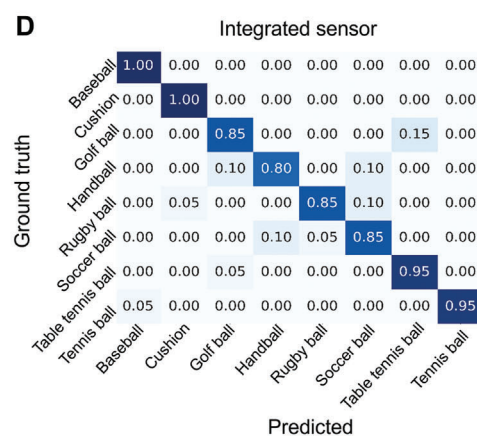
B



C



D



demonstrated that tactile data collected through simple grasping and pressure distribution could achieve an 85.72% accuracy in object recognition, though they noted significant errors when distinguishing objects of similar size and shape. Despite encountering similar challenges, our study achieved improved accuracy, suggesting that the integration of data from three different sensors can enhance object recognition accuracy by leveraging a more diverse set of data inputs.^[4] This discrepancy arises from the limitations of the single Meissner sensor in capturing dynamic stimuli based on vibration and strain when incorporating surface information through rubbing, which is vital for object and surface perception. Consequently, the single Merkel sensor exhibited significantly lower accuracy compared to the integrated sensor. Cases involving combinations like Merkel sensor + Meissner sensor, Merkel sensor + Ruffini sensor, and Meissner sensor + Ruffini sensor demonstrated marginally lower accuracy compared to using a single Merkel sensor alone, emphasizing the necessity of combining Meissner and Ruffini sensors to incorporate additional tactile information related to friction. The current multimodal integration framework demonstrates limitations in complementary information extraction when combining Meissner and Ruffini inputs with the Merkel sensor.^[54–56] Advanced sensor system development requires quantitative characterization of mechanoreceptor-specific contributions to object recognition. Future research directions include detailed characterization of individual mechanoreceptor functionality in multimodal object discrimination tasks. Finally, integrating three types of tactile information—Merkel sensor, Meissner sensor, and Ruffini sensor—resulted in superior accuracy in perceptual functions compared to other combinations, such as Merkel sensor + Meissner sensor, Meissner sensor + Ruffini sensor or single Merkel sensor.

3. Conclusion

In conclusion, this study introduces a pioneering approach in the development of artificial cutaneous mechanoreceptors, drawing inspiration from Merkel discs, Meissner corpuscles, and Ruffini endings to form a comprehensive sensory organ. The integration of three distinct sensors—the Merkel sensor, Meissner sensor, and Ruffini sensor—beneath artificial dermal and epidermal layers proves to be a groundbreaking step in tactile perception. Crucially, the collaborative integration of these sensors offers numerous advantages for object perception compared to using an existing single sensor. The Merkel sensor, with its ion migration response to pressure stimuli, excels in clear decision-making dur-

ing tasks like Braille recognition and object discrimination. The Meissner sensor, addressing pressure and shear forces, collaborates with the Merkel sensor, offering distinctive RA peaks and valuable insights during varied movements. Specializing in skin tension and deformation, Ruffini sensors complement Merkel and Meissner sensors to improve tactile sensation and surface discrimination. While facing challenges in fully reproducing the intricate nature of skin organs, the integrative biomimetic approach proposed in this study shows immense potential. Indeed, the study affirms that leveraging three integrated sensors yields more precise and varied information compared to using one or two sensors for object perception. Consequently, the collaborative synergy among integrated sensors holds the potential to transform the landscape of artificial tactile sensing, offering invaluable benefits for prosthetics, robotics, and virtual/augmented reality applications. This research signifies a substantial technological advancement, enhancing human-machine interaction and charting a course for the creation of artificial tactile sensor systems demanding precise and subtle touch perception.

4. Experimental Section

Preparation of Materials: PVC was purchased from Scientific Polymer Products Inc., and PVDF-TrFe powder was purchased from Piezotech (FC30). DBA was purchased from TCI Chemicals, and (1-ethyl-3-methylimidazolium bis(trifluoromethylsulfonyl)imide), N-Methyl-2-pyrrolidone (NMP), and tetrahydrofuran (THF) used as an ionic liquid were purchased from Sigma-Aldrich. All chemicals were used without purification or pretreatment. MWCNT was purchased from Nanocyl. PVC ion gel was prepared with a weight ratio of PVC/DBA/[EMIM][TFSI] of 1:2:0.2. For PVDF-TrFe gel, the PVDF-TrFe/DBA ratio was 1:2.

Meissner Sensor Fabrication: A mold was crafted to replicate the bump structure of the Meissner sensor, featuring a square design measuring $7 \times 7 \text{ mm}^2$ with a mold depth of 0.5 mm. The center of the mold incorporated a hemispherical groove with a 0.5 mm radius to generate the bump structure. This mold was produced using a 3D printer with UV resin. Following the creation of the mold, $\approx 25 \mu\text{L}$ of PVDF-TrFe solution was filled into it and allowed to dry, resulting in a PVDF-TrFe layer with a bump structure. An Ag layer was then coated onto the PVDF-TrFe layer using sputtering, and electrodes were placed using conductive carbon tape. To enhance electrical contact with the Ag-coated surface, silver paste was applied to the carbon tape. The PVDF-TrFe layer was subsequently filled with Ecoflex 00–30 (1:1 mix) in the mold and at the electrode locations. After curing in an oven at 60°C for $\approx 3 \text{ h}$, the Ecoflex 00–30 with the PVDF-TrFe layer was cut to specifications and removed from the mold.

Flipping the removed fabrication exposed the PVDF-TrFe layer, which was not yet coated with Ag. Following the previous process, Ag coating was performed using sputtering, and electrodes were placed using carbon tape. The silver paste was then applied to reinforce the electrical contact between the electrode and the coated surface. Once the silver paste dried,

Figure 4. Glove sensor and perception experiments with artificial intelligence. A) Glove sensor fabricated with integrated sensors. Each integrated sensor was placed at specific location of finger and palm to perceive tactile information of object touched by the hand. Electrodes from integrated sensors were fixed on surface of the glove with adhesives and aligned on the posterior sides of the hand. The protocol of collecting data was described with schematics. Each trial was conducted for 10 s. A participant gripped each object for 2 s and rubbed the object after gripping. Each rubbing cycle was conducted for 2 s and repeated twice. The schematics of a deep learning architecture comprises 2-layer LSTM with 128 hidden layers and two fully connected layers with 512 and 8 hidden layers, respectively. The objects used are cushion, soccer ball, rugby ball, table tennis ball, baseball, golf ball, tennis ball, and handball. B) Relative comparison of size and surface texture of the objects. The contact area between an object and the glove sensor varied depending on size of the object as described in this diagram. Surface texture was divided into smooth and rough categories. In the classification process by the deep learning architecture, improvement in softmax probability was compared during the 10-s protocol. C) Comparison of accuracy for each combination of tactile information. Data with seven combinations of tactile sensors were compared: integrated sensor, Merkel sensor + Meissner sensor, Merkel sensor + Ruffini sensor, Meissner sensor + Ruffini sensor, Merkel sensor only, Meissner sensor only, Ruffini sensor only. D) Confusion chart of each combination of tactile information from the glove sensor.

a PDMS layer was created by brushing a PDMS 20:1 mixture onto the exposed Ag coating surface. The PDMS layer, with a thickness of ≈ 0.7 mm, was cured in an oven at 60°C for ≈ 3 h, resulting in the final fabrication of the Meissner sensor.

Merkel Sensor Fabrication: The PVC gel, with a fixed weight ratio of PVC/DBA/[EMIM][TFSI] at 1:2:0.2, and the PVDF-TrFe gel, with a PVDF-TrFe/DBA ratio of 1:2, were fabricated. A conical surface structure was achieved through drop-casting using a 3D-printed mold (7×7 mm², depth: 3 mm). Each gel was affixed with double-sided adhesive tape. Electrodes, comprising an Ag wire for PVC and a carbon sheet for PVDF-TrFe, were inserted into the respective gels. To ensure conductivity at the PVC and PVDF-TrFe interface, carbon graphite was applied to the PT gel surface via the spray method. Voltage changes were measured by connecting to an oscilloscope (Tektronix, TDS 2012C), with PVC and PT sides serving as the working and ground sides, respectively.

Ruffini Sensor Fabrication: First, CNT, which acts as a swelling fiber, and internal Ecoflex (Modulus E: ≈ 100 kPa), which acts as a flexible tissue, were complexed. This internal complex is encapsulated to surround the entire conductive complex using an external Ecoflex (Modulus E: ≈ 300 Kpa) with higher rigidity, giving it the role of a Schwann cell layer. NH₂ branched-MWCNTs were used to increase the dispersion of CNTs. MWCNTs were added to NMP at a concentration of $10 \text{ mg } 150 \text{ mL}^{-1}$ and then sonicated for 90 s at a frequency of 16 kHz using a tip sonicator. The membrane filter for the vacuum-based infiltration process used an AAO membrane with a micropore diameter of $47 \mu\text{m}$, and the sufficiently dispersed solution was infiltrated for 1 h. After purification with DI water, MWCNT sheets were obtained through sufficient drying. Afterward, 0.4 ml of Ecoflex was dropped in the center of the sheet and held at a speed of 500 rpm for ≈ 30 s using a high-speed spin coater to spread the polymer evenly over the entire sheet. Afterward, it was placed in a vacuum chamber for ≈ 10 min to allow Ecoflex to infiltrate and then cured at 60°C for 4 h. The composite material was manufactured using a laser-cutting method. It was cut into 6 mm pieces and cured in an oven for 1 min to ensure that the electrodes were securely connected to both ends of the composite. Afterward, the outer Ecoflex, which has a similar composition to the polymer of the composite and has the highest rigidity, was poured (total thickness: 1 mm) and cured in an oven for 4 h to finally complete the Ruffini sensor with a composite capsule structure.

Sensor Characterization: For the application of external force to each sensor, a custom-built system comprising a stepping motor and a force tip was employed. Simultaneously, the output voltage of the sensor was measured by connecting it to a 4-channel oscilloscope (Tektronix, MDO 4024C).

Circuit Architecture: Each integrated sensor has three pairs of carbon tape-based electrodes which was from the Merkel sensor, Meissner sensor, and Ruffini sensor. For the Ruffini sensor, a Wheatstone bridge-based circuit was applied to convert the responses of Ruffini sensor from resistance to electric potential. The bias voltage was set to 0.03 V by external power supply (Keithley, 2400 multimeter), and the other three resistors forming the Wheatstone bridge were all configured as 100Ω .

Fabrication of Glove Sensor: The glove sensor was fabricated utilizing a total of 15 integrated sensors. The allocation of each sensor is specified as follows: For the thumb, a single sensor is positioned at the fingertip. For the index finger, middle finger, ring finger, and little finger, sensors were distributed at three distinct locations: tip of the finger, middle of the finger, and bottom of the finger, with three sensors for each finger. The fingers are numerically designated as follows: thumb as 1, index finger as 2, middle finger as 3, ring finger as 4, and little finger as 5. The respective sensor locations were denominated as t1 for the thumb, t2, t3, t4, t5 for the tips of the fingers, m2, m3, m4, m5 for the middles of the fingers, and b2, b3, b4, b5 for the bottoms of the fingers. Additionally, two sensors located on the palm are labeled as p1 and p2, respectively. After positioning the sensors, they were affixed in place using epoxy adhesive. The ends of the carbon tape, which served as electrodes for the sensors, are oriented to face the posterior side. To prevent the electrodes from making unintended contact or bending, they were subsequently attached and secured to the glove using epoxy adhesive. The carbon tape electrodes lo-

cated on the posterior surface was extended and connected to Cu wires, which were then oriented toward the wrist direction. The fabrication of the glove sensor was completed upon the successful implementation of these steps.

Formation and Manipulation of Glove Sensor: Entire electrodes from integrated sensors attached to glove sensors were 45 wires and each integrated sensor generated signals with tactile information. The integrated sensor attached to the glove sensor consists of a total of 15 units, with each integrated sensor having 3 pairs of electrodes, resulting in a total of 45 electrode pairs connected. Each integrated sensor simultaneously generates three types of tactile data, for which MUX equipment to measure was utilized. (National Instruments, NI 9205, NI cDAQ-9174) The electrodes from the Ruffini sensor was connected to the ports of the MUX via Wheatstone bridge. Dedicated software (National Instruments, DAQ express) was used to process the information collected from the MUX, with a sampling rate set to 100 Hz for each channel. Wearing the glove sensor, experiments were conducted for 10 s each trial, where the actions of grasping and releasing the object were performed during the 2–4 s interval, and the action of stroking the object twice at 2 s intervals was performed during the 4–8 s interval. Data were collected by repeating each category 50 times, conducting repeated experiments for a total of 8 categories including table tennis ball, golf ball, soccer ball, rugby ball, baseball, tennis ball, cushion, and handball.

Data Collecting from a Glove Sensor: In each repeated experiment, the integrated sensors simultaneously collected three types of tactile data: Merkel sensor, Meissner sensor, and Ruffini sensor. To compare the implementation of artificial perceptual functions based on different types of tactile information, LSTM classification training in seven cases was conducted: Merged sensor, Merkel sensor + Meissner sensor, Merkel sensor + Ruffini sensor, Meissner sensor + Ruffini sensor, Merkel sensor only, Meissner sensor only, and Ruffini sensor only. The Merkel sensor only case, Meissner sensor only case, and Ruffini sensor only case were conducted to confirm the functions of single tactile sensors, with particular emphasis on the Merkel sensor only case, which assumes experiments solely based on pressure information, as often conducted in previous studies. Cases such as Merkel sensor + Meissner sensor, Merkel sensor + Ruffini sensor, and Meissner sensor + Ruffini sensor aimed to confirm the effects of combining two or more types of tactile information.

Participant Recruitments: Prior to experimentation, all participating researchers were comprehensively briefed on the experimental protocol, data collection methodologies, and subsequent data utilization. Informed consent was obtained from all participants, ensuring voluntary engagement in the study. The glove-integrated sensor array was designed as a non-invasive, externally worn device, precluding direct contact with the skin or any physical alterations to the body. Consequently, this study was exempt from requiring approval from the Institutional Review Board of the Korea University Bioethics Committee, as per their guidelines for non-invasive, very low-risk human subject research.

Supporting Information

Supporting Information is available from the Wiley Online Library or from the author.

Acknowledgements

S.S., H.-M.N., J.-Y.K., and D.K. contributed equally to this work. The authors acknowledge support from the Basic Science Research Program (RS-2023-00255584) through the National Research Foundation of Korea (NRF) funded by Ministry of Science and ICT (-MSIT) in Korea.

Conflict of Interest

The authors declare no conflict of interest.

Data Availability Statement

The data that support the findings of this study are available on request from the corresponding author. The data are not publicly available due to privacy or ethical restrictions.

Keywords

artificial mechanoreceptor, multimodal, perception, tactile sensor

Received: August 12, 2024

Revised: November 25, 2024

Published online: December 9, 2024

- [1] A. Handler, D. D. Ginty, *Nat. Rev. Neurosci.* **2021**, 22, 521.
- [2] J. E. O'Doherty, M. A. Lebedev, P. J. Ifft, K. Z. Zhuang, S. Shokur, H. Bleuler, M. A. L. Nicolelis, *Nature* **2011**, 479, 228.
- [3] S. S. Ranade, S. H. Woo, A. E. Dubin, R. A. Moshourab, C. Wetzel, M. Petrus, J. Mathur, V. Begay, B. Coste, J. Mainquist, A. J. Wilson, A. G. Francisco, K. Reddy, Z. Qiu, J. N. Wood, G. R. Lewin, A. Patapoutian, *Nature* **2014**, 516, 121.
- [4] S. Sundaram, P. Kellnhofer, Y. Li, J. Y. Zhu, A. Torralba, W. Matusik, *Nature* **2019**, 569, 698.
- [5] B. C.-K. Tee, A. Chortos, A. Berndt, A. K. Nguyen, A. Tom, A. McGuire, Z. C. Lin, K. Tien, W. G. Bae, H. Wang, P. Mei, H. H. Chou, B. Cui, K. Deisseroth, T. N. Ng, Z. Bao, *Science* **2015**, 350, 313.
- [6] K. Y. Chun, Y. J. Son, C. S. Han, *ACS Nano* **2016**, 10, 4550.
- [7] M. L. Jin, S. Park, Y. Lee, J. H. Lee, J. Chung, J. S. Kim, J. S. Kim, S. Y. Kim, E. Jee, D. W. Kim, J. W. Chung, S. G. Lee, D. Choi, H. T. Jung, D. H. Kim, *Adv. Mater.* **2017**, 4, 1605973.
- [8] K. Y. Chun, Y. J. Son, E. S. Jeon, S. Lee, C. S. Han, *Adv. Mater.* **2018**, 30, 1706229.
- [9] M. Ha, S. Lim, S. Cho, Y. Lee, S. Na, C. Baig, H. Ko, *ACS Nano* **2018**, 12, 3964.
- [10] C. Lim, Y. J. Hong, J. Jung, Y. Shin, S. H. Sunwoo, S. Baik, O. K. Park, S. H. Choi, T. Hyeon, J. H. Kim, S. Lee, D. H. Kim, *Sci. Adv.* **2021**, 7, eabd3716.
- [11] S. Chun, J. S. Kim, Y. Yoo, Y. Choi, S. J. Jung, D. Jang, G. Lee, K. I. Song, K. S. Nam, I. Youn, D. Son, C. Pang, Y. Jeong, H. Jung, Y. J. Kim, B. D. Choi, J. Kim, S. P. Kim, W. Park, S. Park, *Nat. Electron.* **2021**, 4, 429.
- [12] D. Jung, C. Lim, H. J. Shim, Y. Kim, C. Park, J. Jung, S. I. Han, S. H. Sunwoo, K. W. Cho, G. D. Cha, D. C. Kim, J. H. Koo, J. H. Kim, T. Hyeon, D. H. Kim, *Science* **2021**, 373, 1022.
- [13] H. Kwon, J. S. Kim, S. Kim, H. Kang, D. J. Kim, H. Choi, D. G. Roe, Y. J. Choi, S. G. Lee, J. H. Cho, D. H. Kim, *Sci. Adv.* **2023**, 9, eadi3827.
- [14] W. Wan, Y. Jiang, D. Zhong, Z. Zhang, S. Choudhury, J. C. Lai, H. Gong, S. Niu, X. Yan, Y. Zheng, C. C. Shih, R. Ning, Q. Lin, D. Li, Y. H. Kim, J. Kim, Y. X. Wang, C. Zhao, C. Xu, X. Ji, Y. Nishio, H. Lyu, J. B. H., Z. B. Tok, *Science* **2023**, 380, 735.
- [15] D. Deflorio, M. Di Luca, A. M. Wing, *Front. Hum. Neurosci.* **2022**, 16, 862344.
- [16] A. Zimmerman, L. Bai, D. D. Ginty, *Science* **2014**, 346, 950.
- [17] A. Chortos, J. Liu, Z. Bao, *Nat. Mater.* **2016**, 15, 937.
- [18] B. B. Edin, G. K. Essick, M. Trulsson, K. A. Olsson, *J. Neurosci.* **1995**, 15, 830.
- [19] S. H. Kim, Y. H. Lee, *Anat. Cell Biol.* **2020**, 53, 325.
- [20] M. Paré, R. Elde, J. E. Mazurkiewicz, A. M. Smith, F. L. Rice, *J. Neurosci.* **2001**, 21, 7236.
- [21] J. Garcia-Piqueras, R. Cobo, L. Carcaba, Y. Garcia-Mesa, J. Feito, J. Cobo, *O. J. Anat.* **2020**, 236, 854.
- [22] I. Suazo, J. A. Vega, Y. Garcia-Mesa, J. Garcia-Piqueras, O. Garcia-Suarez, T. Cobo, *Front. Neurosci.* **2022**, 16, 790130.
- [23] J. Hao, C. Bonnet, M. Amsalem, J. Ruel, P. Delmas, *Pflugers. Arch. Eur. J. Physiol.* **2015**, 467, 109.
- [24] V. E. Abaira, D. D. Ginty, *Neuron* **2013**, 79, 618.
- [25] H. Q. Huynh, T. Q. Trung, A. Bag, T. D. Do, M. J. Sultan, M. Kim, N. E. Lee, *Adv. Funct. Mater.* **2023**, 33, 2303535.
- [26] Y. Gao, B. Zhang, Y. Liu, K. Yao, X. Huang, J. Li, T. H. Wong, Y. Huang, J. Li, M. Wu, H. Li, Z. Gao, W. Park, C. K. Yiu, H. Jia, R. Shi, D. Li, X. Yu, *Adv. Mater. Technol.* **2023**, 8, 2200759.
- [27] J. Su, H. Zhang, H. Li, K. He, J. Tu, F. Zhang, Z. Liu, Z. Lv, Z. Cui, Y. Li, J. Li, L. Z. Tang, X. Chen, *Adv. Mater.* **2024**, 36, 2311549.
- [28] S. Maksimovic, M. Nakatani, Y. Baba, A. M. Nelson, K. L. Marshall, S. A. Wellnitz, P. Firozi, S. H. Woo, S. Ranade, A. Patapoutian, E. A. Lumpkin, *Nature* **2014**, 509, 617.
- [29] P. Delmas, J. Hao, L. Rodat-Despoix, *Nat. Rev. Neurosci.* **2011**, 12, 139.
- [30] B. U. Hoffman, Y. Baba, T. N. Griffith, E. V. Mosharov, S. H. Woo, D. D. Roybal, G. Karsenty, A. Patapoutian, D. Sulzer, E. A. Lumpkin, *Neuron* **2014**, 100, 1401.
- [31] J. S. Kim, H. Choi, H. J. Hwang, D. Choi, D. H. Kim, *Macromol. Biosci.* **2020**, 20, 2070023.
- [32] Y. Dobashi, D. Yao, Y. Petel, T. N. Nguyen, M. S. Sarwar, Y. Thabet, C. L. W. Ng, E. S. Glitz, G. T. M. Nguyen, C. Plesse, F. Vidal, C. A. Michal, J. D. W. Madden, *Science* **2022**, 376, 502.
- [33] K. Y. Chun, S. Seo, *ACS Sens.* **2021**, 6, 1940.
- [34] H. J. Lee, K. Y. Chun, J. H. Oh, C. S. Han, *ACS Sens.* **2021**, 6, 2411.
- [35] K. Y. Chun, S. Seo, C. S. Han, *Adv. Mater.* **2022**, 34, 2110082.
- [36] D. Choi, S. Jang, J. S. Kim, H. J. Kim, D. H. Kim, J. Y. Kwon, *Adv. Mater. Technol.* **2019**, 4, 1800284.
- [37] V. Amoli, J. S. Kim, E. Jee, Y. S. Chung, S. Y. Kim, J. Koo, H. Choi, Y. Kim, D. H. Kim, *Nat. Commun.* **2019**, 10, 4019.
- [38] E. K. Boahen, B. Pan, H. Kwon, J. S. Kim, H. Choi, Z. Kong, D. J. Kim, J. Zhu, W. B. Ying, K. J. Lee, D. H. Kim, *Nat. Commun.* **2022**, 13, 7699.
- [39] N. L. Neubarth, A. J. Emanuel, Y. Liu, M. W. Springel, A. Handler, Q. Zhang, B. P. Lehnert, C. Guo, L. L. Orefice, A. Abdelaziz, M. M. DeLisle, M. Iskols, J. Rhynis, S. J. Kim, S. J. Cattel, W. Regehr, C. D. Harvey, J. Drugowitsch, D. D. Ginty, *Science* **2020**, 368, 1330.
- [40] T. Maeno, K. Kobayashi, N. Yamazaki, *JSME Int. J. Series C* **1998**, 41, 94.
- [41] S. Kuroki, H. Kajimoto, H. Nii, N. Kawakami, S. Tachi, *Haptics: Perception, Devices and Scenarios*, Springer, Berlin, Germany **2008**.
- [42] M. S. Fleming, W. Luo, *Front. Biol.* **2013**, 8, 408.
- [43] M. Paré, C. Behets, O. Cornu, *J. Comparat. Neurol.* **2003**, 456, 260.
- [44] R. Cobo, Y. Garcia-Mesa, L. Carcaba, J. Martin-Cruces, J. Feito, O. Garcia-Suarez, J. Cobo, J. Garcia-Piqueras, J. A. Vega, *J. Anatomy* **2021**, 238, 13.
- [45] J. Oh, J. C. Yang, J. O. Kim, H. Park, S. Y. Kwon, S. Lee, J. Y. Sim, H. W. Oh, J. Kim, S. Park, *ACS Nano* **2018**, 12, 7546.
- [46] D. F. Collins, K. M. Refshauge, S. C. Gandevia, *J. Physiol.* **2000**, 529, 505.
- [47] J. C. Tuthill, E. Azim, *Curr. Biol.* **2018**, 28, R194.
- [48] J. R. Phillips, R. S. Johansson, K. O. Johnson, *J. Neurosci.* **1992**, 12, 827.
- [49] J. R. Phillips, R. S. Johansson, K. O. Johnson, *Exp. Brain Res.* **1990**, 81, 589.
- [50] G. Westling, R. S. Johansson, *Exp. Brain Res.* **1987**, 66, 128.
- [51] N. Bai, Y. Xue, S. Chen, L. Shi, J. Shi, Y. Zhang, X. Hou, Y. Cheng, K. Huang, W. Wang, J. Zhang, Y. Liu, C. F. Guo, *Nat. Comm.* **2023**, 14, 7121.
- [52] Y. Luo, X. Xiao, J. Chen, Q. Li, H. Fu, *ACS Nano* **2022**, 16, 6734.
- [53] J. Man, Z. Jin, J. Chen, *Adv. Sci.* **2024**, 11, 2306832.
- [54] H. Niu, H. Li, S. Gao, Y. Li, X. Wei, Y. Chen, W. Yue, W. Zhou, G. Shen, *Adv. Mater.* **2022**, 24, 202202622.
- [55] Z. Liu, X. Hu, R. Bo, Y. Yang, X. Cheng, W. Pang, Q. Liu, Y. Wang, S. Wang, S. Xu, Z. Shen, Y. Zhang, *Science* **2024**, 384, 987.
- [56] S. Chun, J.-S. Kim, Y. Yoo, Y. Choi, S. J. Jung, D. Jang, G. Lee, K.-I. Song, K. S. Nam, I. Youn, D. Son, C. Pang, Y. Jeong, H. Jung, Y.-J. Kim, B.-D. Choi, J. Kim, S.-P. Kim, W. Park, S. Park, *Nat. Electron.* **2021**, 4, 429.